Contents lists available at ScienceDirect

Arabian Journal of Chemistry

journal homepage: www.ksu.edu.sa

Original article

Magnetic photocatalyst $Bi_3O_4Cl/Mn_xZn_{1-x}Fe_2O_4$: Facile synthesis and its photocatalytic activity

Hailong Wang [a,b,*], Dan Yang [a], Longjun Xu [b,*]

[a] College of Engineering, Sichuan Normal University, Chengdu 610101, Sichuan, China
[b] State Key Laboratory of Coal Mine Disaster Dynamics and Control, Chongqing University, Chongqing 400044, China

ARTICLE INFO

Keywords:
$Bi_3O_4Cl/Mn_xZn_{1-x}Fe_2O_4$
Hydrothermal-roasting method
Photocatalytic activity
Magnetic recovery

ABSTRACT

Herein, a $Bi_3O_4Cl/Mn_xZn_{1-x}Fe_2O_4$ composite photocatalyst based on $Mn_xZn_{1-x}Fe_2O_4$ is fabricated by hydrothermal and roasting methods. The performances of the obtained photocatalysts were detected via XRD, SEM, EDS, TEM, UV–vis, PL and nitrogen absorption-desorption equipment, which indicated the successful combination of nanosheet Bi_3O_4Cl and granular $Mn_xZn_{1-x}Fe_2O_4$. The activity of the photocatalyst was investigated under solar light with rhodamine B (RhB) as a simulated pollutant, which achieved high catalytic and magnetic properties. In addition, 99.5 % degradation of RhB was displayed by MB-10(10 %$Mn_xZn_{1-x}Fe_2O_4/Bi_3O_4Cl$). The $Bi_3O_4Cl/Mn_xZn_{1-x}Fe_2O_4$ photocatalyst was regarded as having excellent kinetic properties for recycling and magnetism due to its low hysteresis loss illustrated in the hysteresis loop images. In addition, the average recovery of the samples was 91.3 %, which successfully verified the excellent stability of the composites in RhB degradation. This paper demonstrates that the doping of magnetic material onto Bi_3O_4Cl is a feasible approach to remove RhB. The recovery of the photocatalyst, which provides low cost and highly efficient photocatalysis, is guiding a brand-new strategy for the elimination of organic contaminants.

1. Introduction

The development of society has led to an increased consumption of products to improve people's quality of life (Hu et al., 2020). However, the use of a large number of environmentally toxic dyes is usually overshadowed by the pleasing consumption, which causes the retention of contamination in the environment, resulting in irreparable consequences (Ma et al., 2020; Ma et al., 2020; Jing et al., 2020; Niu et al., 2020; Frindy and Sillanpää, 2020). Thus, the elimination of toxic dyes is crucial. Physical absorption, ion exchange, chemical and biological oxidation, biodegradation, photoelectrocatalysis, membrane filtration, coagulation and adsorption have been utilized to remove dyes such as RhB throughout history (Zhang et al., 2020; Wang et al., 2021; Khalid et al., 2020; Ghorai et al., 2021; Luo et al., 2020; Bao et al., 2021; Cainglet et al., 2020; Zhao et al., 2023; Sohrabi and Ameri, 2015). However, there are still dyes remaining in the environment even after the processes listed, causing severe damage to Earth. Thus, the elimination of dyes has become a hot topic, and numerous studies have presented a practical solution.

Photocatalysts, which have been confirmed to decompose dyes to small molecules by direct light activation, are ideal candidates to remove aquatic pollutants due to their low cost, ease of control and environmental friendliness (Acharya et al., 2020; Li et al., 2020; Wang et al., 2020; Talreja et al., 2021; Behnood and Sodeifian, 2021; Bhatt et al., 2021; Ye et al., 2021; Cui et al., 2021; Sharma et al., 2020; Sun et al., 2018; Senthil et al., 2019). Titanium dioxide has been widely investigated due to its acute photocatalytic activity, photostability and nontoxicity (Nabi et al., 2021; Li et al., 2020; Ziental et al., 2020; Pan et al., 2020; Eddy et al., 2021). However, the photocatalytic reaction of titanium dioxide only occurs in the ultraviolet excitation band, and the recombination of holes and electrons results in low quantum efficiency, which leads to the weak activity of TiO2 (Li et al., 2021; Pant et al., 276 (2021); Li et al., 2021). Akyüz (Akyüz, 2021) successfully prepared a rGO-TiO_2-CdO-ZnO-Ag composite photocatalyst under the sol–gel method, which displayed preferable photocatalytic activity than pristine TiO_2 in condition of visible light irradiation. Zhao et al. (Zhao et al., 2021) first prepared numerous self-assembled WO_3-decorated TiO_2 nanocrystallites with the combination of strategic integration and membrane water filtration to identify the magnetic behaviour and photocatalytic activity. However, due to the difficulty of recovery, the

* Corresponding authors.
E-mail addresses: cqwhl@sicnu.edu.cn (H. Wang), xulj@cqu.edu.cn (L. Xu).

https://doi.org/10.1016/j.arabjc.2024.105699
Received 25 November 2023; Accepted 26 February 2024
Available online 29 February 2024

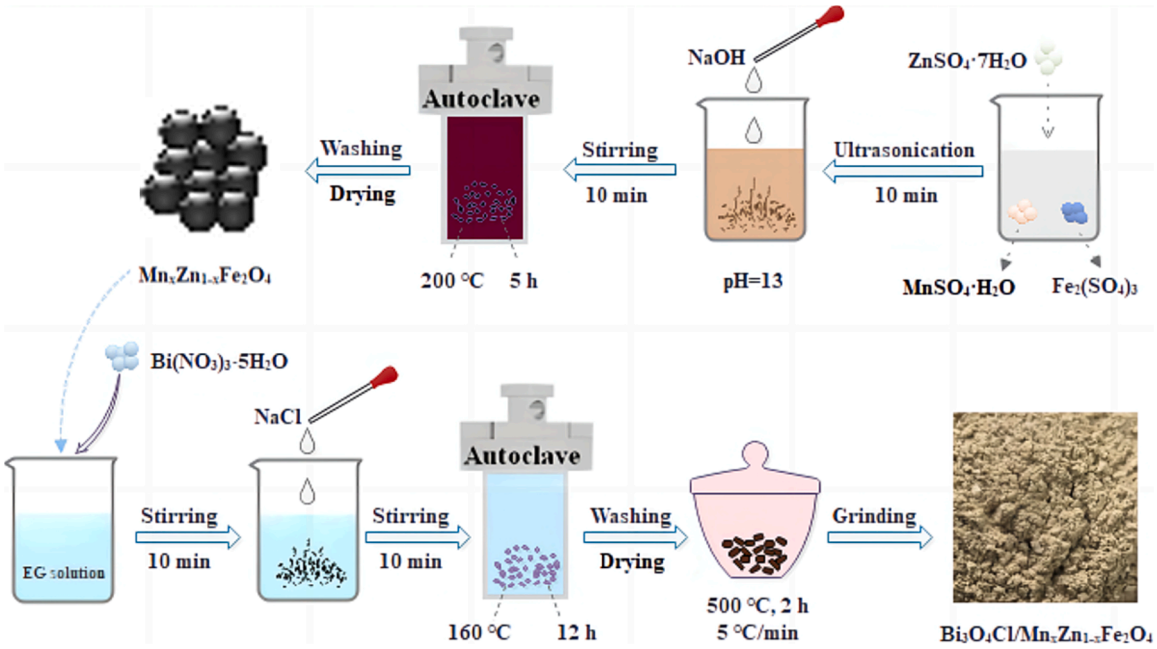

Fig. 1. Preparation flow of $Bi_3O_4Cl/Mn_xZn_{1-x}Fe_2O_4$.

environment would suffer great pollution by modified TiO_2 photocatalysts. In addition, the minimization of cost leads to the recovery of the photocatalyst after utilization, and $Mn_xZn_{1-x}Fe_2O_4$ is prepared to enhance the photocatalytic activity and magnetic recovery rate (Cheng et al., 2021; Jiang et al., 2021). To meet the ideal outcome, a new photocatalyst has been investigated.

Wrapped by two chlorine atoms, the unique layered structure of Bi_3O_4Cl has attracted extensive interest. As a member of Silén, the superior photocatalytic efficiency Bi_3O_4Cl displayed in the inner electrostatic field perpendicular to the laminar layer, which promotes greater segregation of photogenerated electron-hole pairs. Xu (Xu et al., 2020) prepared Bi_3O_4Cl by calcining Bi_2O_3 and BiOCl under high temperature, which presented high photocatalytic degradation efficiency under visible light irradiation. Notably, Yuan (Yuan et al., 2022) successfully prepared the S-scheme $Bi_7O_9I_3$/g-C_3N_4/Bi_3O_4Cl composite photocatalyst by an oil bath method, which exhibited better photocatalytic degradation efficiency than pure Bi_3O_4Cl. However, these studies exhibited tedious steps and high energy consumption in preparation. Moreover, for the sake of cost reduction, any photocatalyst should be recoverable, and the general application to add magnetic material in the preparation of composite photocatalyst. That is, the photocatalytic degradation efficiency could be improved by recycling magnetism in a magnetic composite photocatalyst.

In this work, Bi_3O_4Cl prepared by a hydrothermal-roasting method could be a rapid, simple and effective synthesis pathway. In addition, $Mn_xZn_{1-x}Fe_2O_4$, known as a typical soft magnetic material, exhibits an effective saturation magnetization, perfect permeability, low loss, high stability, and an ideal recycling efficiency (Cheng et al., 2021). Additionally, since it is used as a magnetic substance, the combination of Bi_3O_4Cl and $Mn_xZn_{1-x}Fe_2O_4$ could be an ideal candidate to meet the demands. Herein, $Bi(NO_3)_3{\cdot}5H_2O$ and NaCl were utilized as raw materials to prepare Bi_3O_4Cl by a hydrothermal method, and $Mn_xZn_{1-x}Fe_2O_4$ was added into the combination. Thus, a $Bi_3O_4Cl/Mn_xZn_{1-x}Fe_2O_4$ magnetic composite photocatalyst was prepared, which presents an effective and simple method for the preparation of Bi_3O_4Cl, promoting the application and development of photocatalytic technology in controlling environmental pollution.

2. Experimental

2.1. Experimental materials

Chengdu Kelong Chemical Co., Ltd. (Chengdu, China) purchased $Bi(NO_3)_3{\cdot}5H_2O$, NaCl, NaOH, $ZnSO_4{\cdot}7H_2O$, $MnSO_4{\cdot}H_2O$, $Fe_2(SO_4)_3$, and $C_2H_6O_2$. It is noteworthy that all chemical reagents were of analytical grade and can be used directly without any purification.

2.2. Preparation of $Bi_3O_4Cl/Mn_xZn_{1-x}Fe_2O_4$

Herein, by the application of hydrothermal and roasting methods, bismuth oxychloride/manganese and zinc ferrite ($Bi_3O_4Cl/Mn_xZn_{1-x}Fe_2O_4$) composite photocatalysts were synthesized by preparing $Bi(NO_3)_3{\cdot}5H_2O$ and NaCl as raw materials and preparing $Mn_xZn_{1-x}Fe_2O_4$ as an additive. It was synthesized by the following procedures presented in Fig. 1. First, a certain amount of $ZnSO_4{\cdot}7H_2O$, $MnSO_4{\cdot}H_2O$, and $Fe_2(SO_4)_3$ mixed solution was dissolved in distilled water and stirred ultrasonically for 10 min. Then 2 mol/L sodium hydroxide solution was added dropwise. The pH of the solution was adjusted to 13 and stirred for 10 min. Then the mixed solution was placed in a high-pressure reactor at 200 °C for 5 h. After washing and drying, the $Mn_xZn_{1-x}Fe_2O_4$ magnetic matrix was obtained.Then, 20 mL of ethylene glycol, 0.97 g of $Bi(NO_3)_3{\cdot}5H_2O$ were mixed into a beaker and sonicated for 10 min. $Mn_xZn_{1-x}Fe_2O_4$ accounting for 5 %~25 % of the total mass were added into the levitated solution and mechanically stirred for 10 min. After that, 50 mL of NaCl (0.0134 mol/L) was added dropwise to the levitated solution. After stirred for 10 min again, the mixture was calcined at 160 °C for 12 h to obtain the intermediate product in the reaction at room temperature. The specimens were scrubbed with anhydrous ethanol and aqua destillata many times and desiccated at 75 °C for 12 h. The samples were ground into 100 mL ceramic crucible, continuously roasted at 500 °C for 2 h and ground to obtain $Bi_3O_4Cl/Mn_xZn_{1-x}Fe_2O_4$ at room temperature. In addition, 5 % ~ 25 % $Mn_xZn_{1-x}Fe_2O_4/Bi_3O_4Cl$ were named MB-5, MB-10, MB-15, MB-20, and MB-25, respectively.

2.3. Characterization

The phase structure and crystallographic structure of the $Bi_3O_4Cl/$

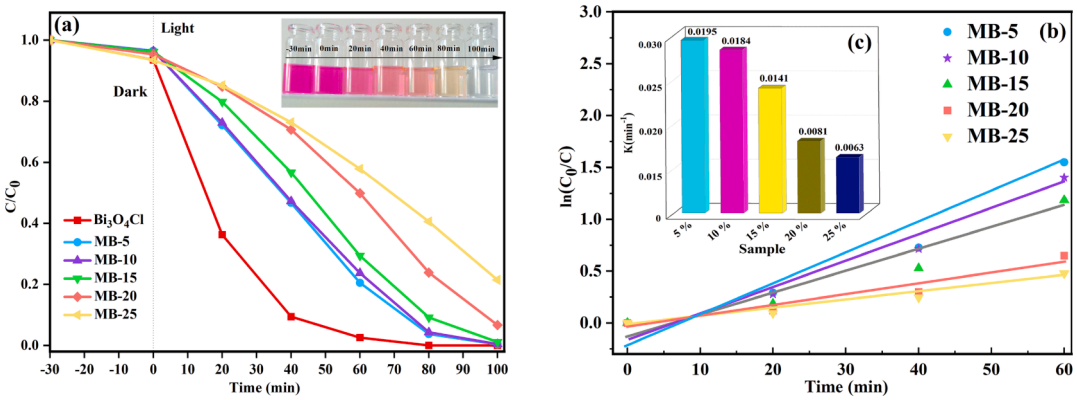

Fig. 2. **(a)** Photocatalytic degradation; **(b)** kinetic linear simulation curves of RhB over Bi_3O_4Cl and $Bi_3O_4Cl/Mn_xZn_{1-x}Fe_2O_4$; **(c)** values of reaction rate constants.

$Mn_xZn_{1-x}Fe_2O_4$ composite photocatalyst were obtained by X-ray diffraction (Shimadzu XRD 6000, Japan) with monochromated high-intensity Cu Ka radiation. The surface appearance of the composites was characterized by SEM (S4800, Japan). Through TEM (Tecnai G2 F20, USA), the appearance and microstructure of the samples were further displayed. A specific surface and aperture analyser (Quadrasorb 2 MP, USA), which was applied to analyse the composites, exhibited the specific surface area (BET). In addition, UV–vis diffuse reflectance spectra (DRS) were acquired on a Shimadzu UV-2600 UV–Vis spectrophotometer (TU-1901, China). With excitation at a wavelength of 380 nm, photoluminescence (PL) spectra of the powder samples were recorded with a fluorescence spectrophotometer (F-4700, Japan). Furthermore, electrochemical impedance spectroscopy (EIS, CHI660E, CHI Shanghai, Inc.) were utilized to confirm the separation efficiency and interfacial charge transfer of the $Bi_3O_4Cl/Mn_xZn_{1-x}Fe_2O_4$ composite photocatalyst.

2.4. Photocatalytic evaluation

RhB was applied as a simulated dye wastewater, which evaluated the degradation activity of the photocatalytic composite under irradiation with visible light. The simulated pollutant (10 mg/L) was prepared with the addition of 100 mg photocatalyst and placed into darkness for 30 min with stirring to achieve adsorption equilibrium. At ten-minute intervals, the absorbance was measured during the photodegradation process under a xenon lamp (CEL-HXF300-T3, China). The photodegradation process could be presented via a pseudofirst-order reaction under low RhB conditions, which follows the formula,

$$ln(C0/Ct) = kt \quad (1)$$

where, C_0 and C_t represent the average concentration before and after illumination, respectively, while k exhibits the apparent rate constant.

3. Results and discussion

3.1. Photocatalytic activity

Photocatalytic performance of the photocatalyst was measured under simulated solar light irradiation, as illustrated in Fig. 2(a). In 100 min, the degradation rates of MB-5, MB-10, MB-15, MB-20, and MB-25

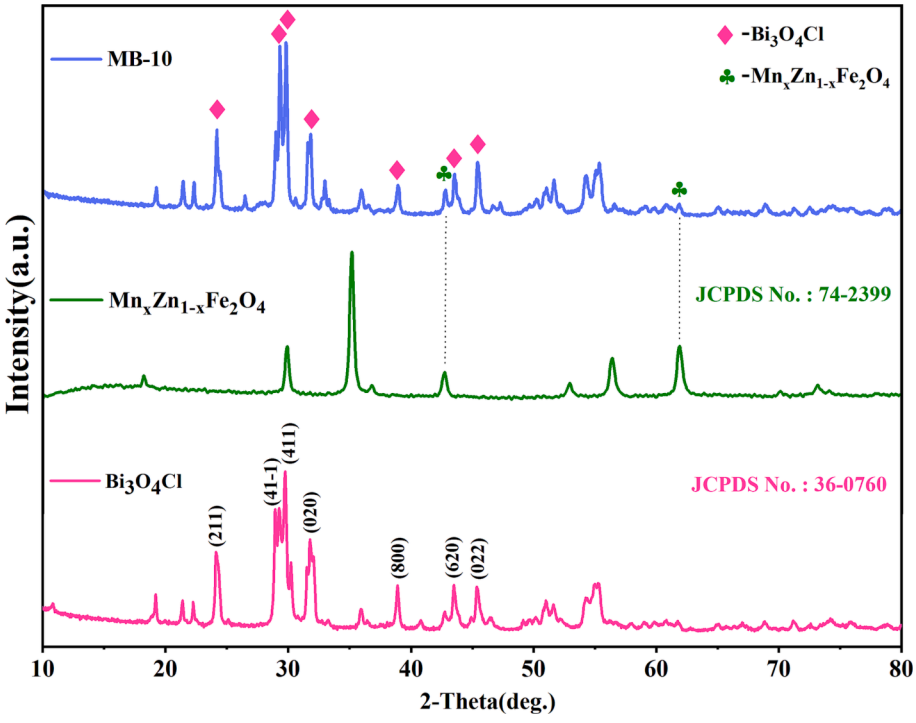

Fig. 3. XRD patterns of Bi_3O_4Cl, $Mn_xZn_{1-x}Fe_2O_4$ and MB-10.

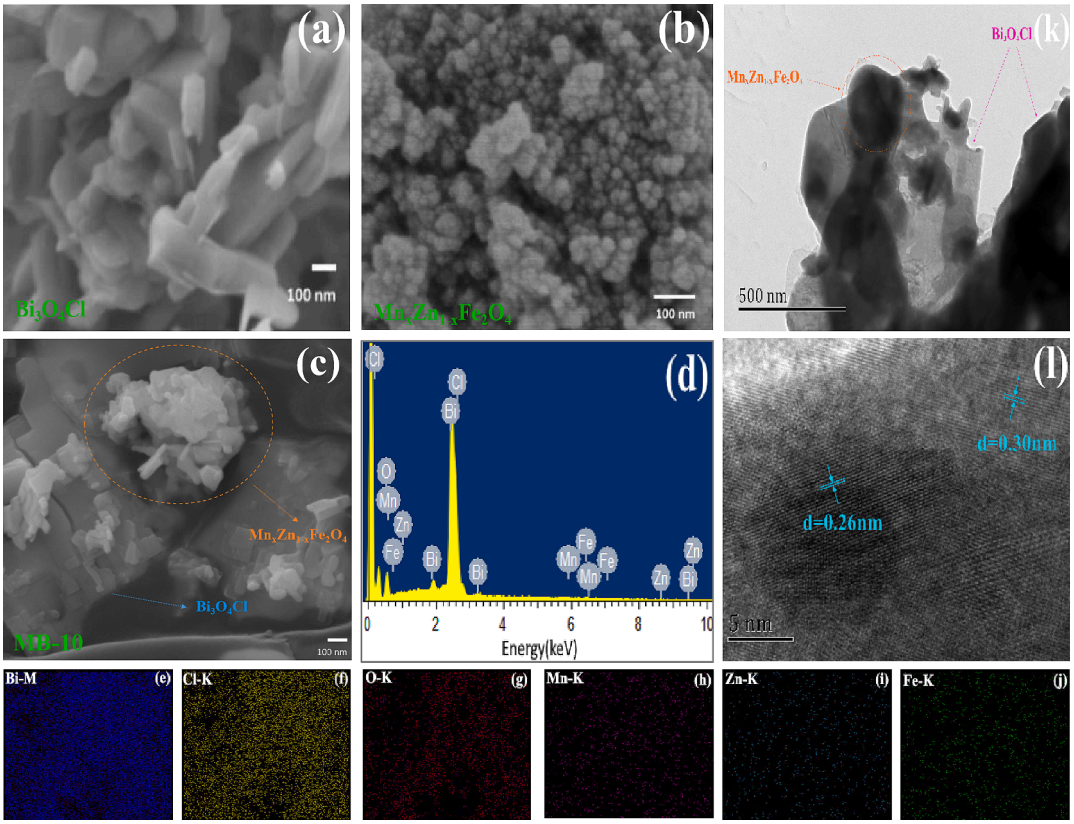

Fig. 4. **(a)-(c)** SEM images of Bi_3O_4Cl, $Mn_xZn_{1-x}Fe_2O_4$ and MB-10; **(d)** EDS spectrum of MB-10; **(e)-(j)** EDS elemental mapping of Bi, Cl, O, Mn, Zn and Fe; **(k)** TEM image of MB-10; **(l)** HRTEM image of MB-10.

for RhB were 99.6 %, 99.5 %, 98.9 %, 93.3 % and 78.5 %, respectively. The kinetic model analysis confirmed that the degradation of RhB by the $Bi_3O_4Cl/Mn_xZn_{1-x}Fe_2O_4$ composite magnetic photocatalyst met the first-order reaction kinetics model. MB-5 exhibited perfect photocatalytic degradation of RhB with 0.0195 min^{-1}. MB-10 displayed weaker catalytic degradation but outperformed MB-5 in magnetic recovery, which was chosen as the best candidate to be test analysed.

3.2. Structure characteristics

The crystalline formation of the composites could be investigated via X-ray diffraction (XRD) patterns shown in Fig. 3. The different peaks of Bi_3O_4Cl and $Mn_xZn_{1-x}Fe_2O_4$ were indexed to monoclinic Bi_3O_4Cl (JCPDS No.: 36-0760) and cubic $Mn_xZn_{1-x}Fe_2O_4$ (JCPDS No.: 74-2399), respectively. The diffraction peaks at $2\theta = 24.31°$, 29.13°, 29.68°, 31.65°, 38.77°, 43.36° and 45.25° could be perfectly indexed to monoclinic Bi_3O_4Cl. By the Scherrer formula, the mean grain size of Bi_3O_4Cl was determined to be 29.9 nm. Compared with pristine Bi_3O_4Cl, the appearance of characteristic peaks associated with Bi_3O_4Cl in $Bi_3O_4Cl/Mn_xZn_{1-x}Fe_2O_4$ and the characteristic peaks at $2\theta = 29.91°$, 42.94° and 62.01° corresponding to $Mn_xZn_{1-x}Fe_2O_4$ could still be recognized, confirming the successful incorporation of $Mn_xZn_{1-x}Fe_2O_4$ onto Bi_3O_4Cl.

The surface morphologies of the samples are observed via SEM and EDS mapping, as presented in Fig. 4. Compared with granular $Mn_xZn_{1-x}Fe_2O_4$, Bi_3O_4Cl showed irregular nanosheets. SEM and EDS mapping of the results revealed the combination of Bi_3O_4Cl and $Mn_xZn_{1-x}Fe_2O_4$,

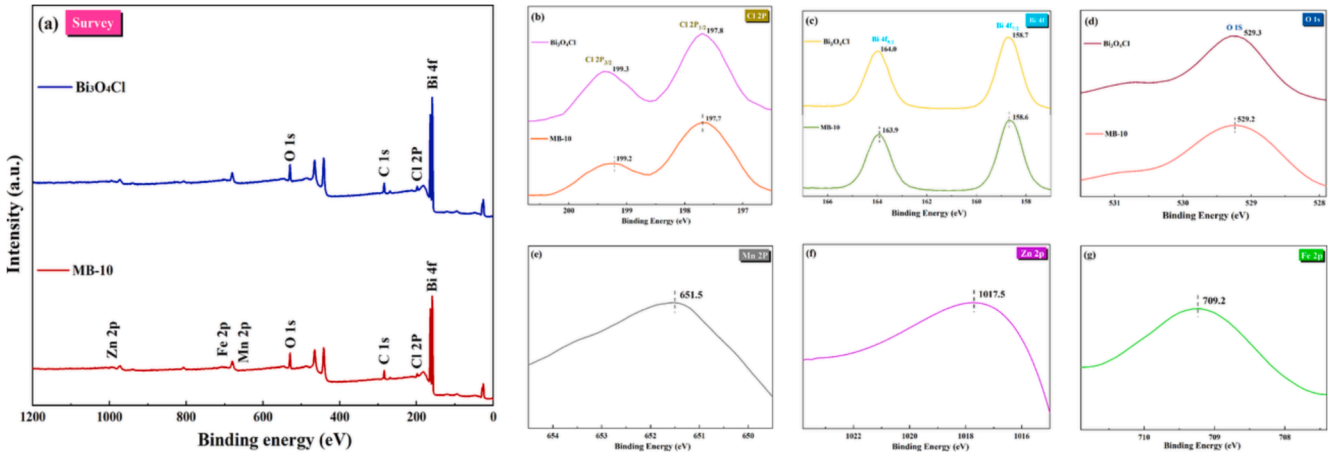

Fig. 5. **(a)** X-ray photoelectron spectroscopy (XPS) survey spectra; **(b–g)** corresponding high-resolution XPS spectra of each element.

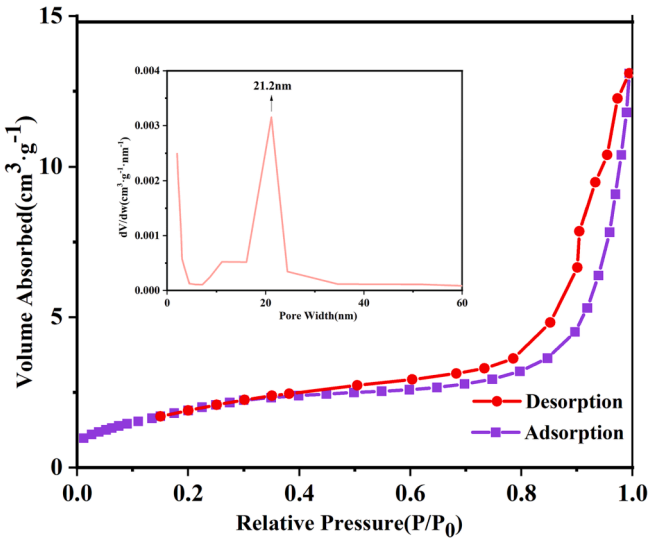

Fig. 6. The N_2 adsorption-desorption isotherms of MB-10 (Inset is pore diameter distribution curve).

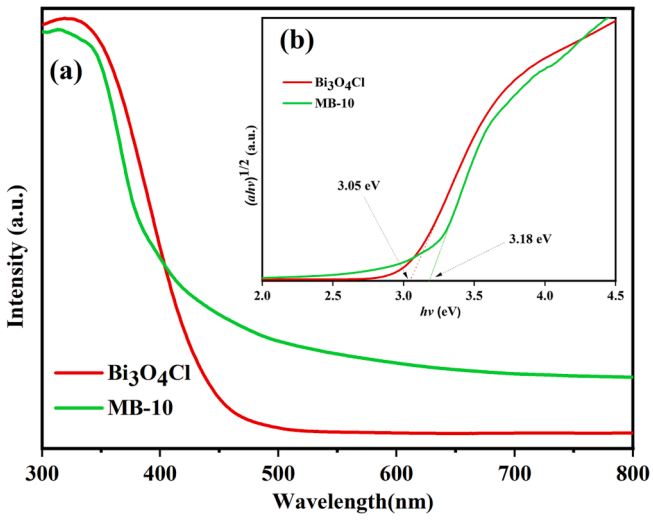

Fig. 7. (a) UV–vis DRS of Bi_3O_4Cl and MB-10; **(b)** The $(ahv)^{1/2}$-hv curve of Bi_3O_4Cl and MB-10.

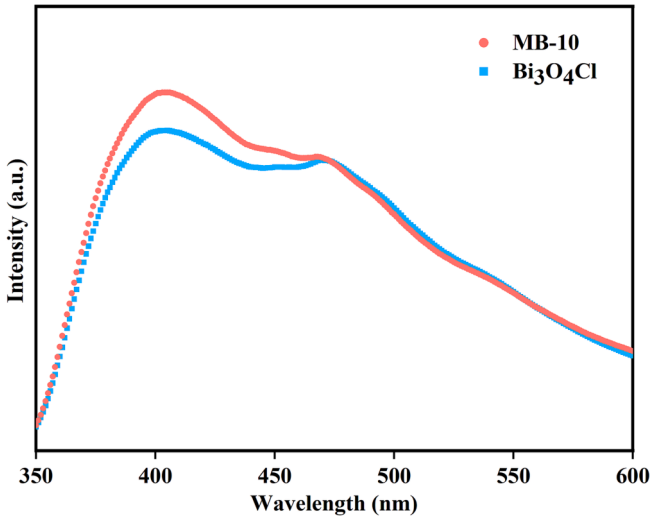

Fig. 8. PL emission spectra of Bi_3O_4Cl和MB-10.

corresponding to XRD. Only Bi, Cl, O, Mn, Zn and Fe were uniformly distributed in the composite. These results indicate that the $Bi_3O_4Cl/Mn_xZn_{1-x}Fe_2O_4$ composite photocatalysts obtained were pure.

Transmission electron microscopy (TEM) is used to express the surface morphologies of $Bi_3O_4Cl/Mn_xZn_{1-x}Fe_2O_4$. The TEM images of the $Bi_3O_4Cl/Mn_xZn_{1-x}Fe_2O_4$ composite photocatalyst investigated in Fig. 4 (k) confirm the doping of $Mn_xZn_{1-x}Fe_2O_4$ onto Bi_3O_4Cl shown in SEM. The HRTEM exhibited in Fig. 4(l) shows a spacing of 0.26 nm and a crystal lattice fringe spacing of 0.30 nm, identified with (411) crystal Bi_3O_4Cl and (311) crystal $Mn_xZn_{1-x}Fe_2O_4$, respectively. This clearly exhibits the differences between each crystal plane and confirms the successful preparation of the $Bi_3O_4Cl/Mn_xZn_{1-x}Fe_2O_4$ compound.

The chemical composition of support surface of MB-10, which was surveyed by XPS survey spectra, proving the constitution and chemical shift of of Bi_3O_4Cl and $Mn_xZn_{1-x}Fe_2O_4$. According to Fig. 5(a), MB-10 exhibits all elements of Bi, Cl, Mn, O, Zn, C, and Fe, which are in consistent with the HRTEM and EDS outcomes. The spectrum of Cl 2P could be separated into two characteristic peaks at 199.2 eV (Cl $2P_{3/2}$) and 197.7 eV (Cl $2P_{1/2}$), indicating the existence of Cl^- (Zhou et al., 2018). In the meantime, the characteristic peaks at 163.9 eV (Bi $4f_{5/2}$) and 158.6 eV (Bi $4f_{7/2}$) in the Bi 4f spectrum confirmed the existent form of Bi^{3+} (Li et al., 2018). The O 1s spectrum can fit the characteristic peak at 529.2 eV illustrated in Fig. 5(d). The major peaks at 651.5 eV, 709.2 eV, and 1017.5 eV in Mn 2p, Fe 2p and Zn 2p spectrum are attributed to $Mn_xZn_{1-x}Fe_2O_4$ presented in Fig. 5(e-g). Moreover, the peaks of O 1s, Bi 4f and Br 3d in MB-10 slightly shift to the weaker binding energy direction through the intense interaction between Bi_3O_4Cl and $Mn_xZn_{1-x}Fe_2O_4$ (compared to pure Bi_3O_4Cl). In summary, the interface between Bi_3O_4Cl and $Mn_xZn_{1-x}Fe_2O_4$ is formed by chemical interactions rather than simple physical mixing.

The aperture partition and Brunauer–Emmett–Teller surface area (S_{BET}) of the $Bi_3O_4Cl/Mn_xZn_{1-x}Fe_2O_4$ magnetic composite photocatalyst were investigated by N_2 adsorption and desorption isotherms, as exhibited in Fig. 6. The whole specimens were presented typical Type IV isotherms, indicating the presence of mesoporous within the production. At higher relative pressures P/P_0, type H_3 hysteresis loop was observed, suggesting the existence of slit-shaped macropores. Fig. 6 illustrates the pore size distribution of the $Bi_3O_4Cl/Mn_xZn_{1-x}Fe_2O_4$ composite photocatalyst, and the most likely pore size distribution is 21.2 nm. The total pore volume of $Bi_3O_4Cl/Mn_xZn_{1-x}Fe_2O_4$ was 0.0203 cm^3/g. The S_{BET} values of $Bi_3O_4Cl/Mn_xZn_{1-x}Fe_2O_4$ and Bi_3O_4Cl were 7.27 and 5.82 m^2/g, respectively. Typically, the superior specific surface area of the photocatalysts was essential to higher adsorption of RhB, since more active loci could be furnished.

3.3. Optical properties

Upon UV–vis diffuse reflection spectra, the photoresponsibility of the $Bi_3O_4Cl/Mn_xZn_{1-x}Fe_2O_4$ composite photocatalyst and Bi_3O_4Cl are investigated in Fig. 7(a). UV and visible light could be absorbed by both. In comparison with pristine Bi_3O_4Cl, the $Bi_3O_4Cl/Mn_xZn_{1-x}Fe_2O_4$ composite photocatalyst absorbed a smaller wavelength of 420 nm, which demonstrated a narrower response range for visible light of the $Bi_3O_4Cl/Mn_xZn_{1-x}Fe_2O_4$ composite photocatalyst leading to weaker photocatalytic activity.

The $(ahv)^{1/2}$-hv images are obtained in Fig. 7(b) since Bi_3O_4Cl is an indirect band gap semiconductor (Lin et al., 2006). Band gap energy (Eg) is shown at the intersection point of the curve tangent extension line and the abscissa axis. The calculated results indicated that the $E_{g\ values}$ of Bi_3O_4Cl and $Bi_3O_4Cl/Mn_xZn_{1-x}Fe_2O_4$ were 3.05 eV and 3.18 eV, respectively. Compared with Bi_3O_4Cl, $Bi_3O_4Cl/Mn_xZn_{1-x}Fe_2O_4$ composite photocatalysts exhibited a higher band gap energy, which indicates that the greater difficulty in yielding electrons and holes than Bi_3O_4Cl was responsible for the weaker photocatalytic activity of $Bi_3O_4Cl/$

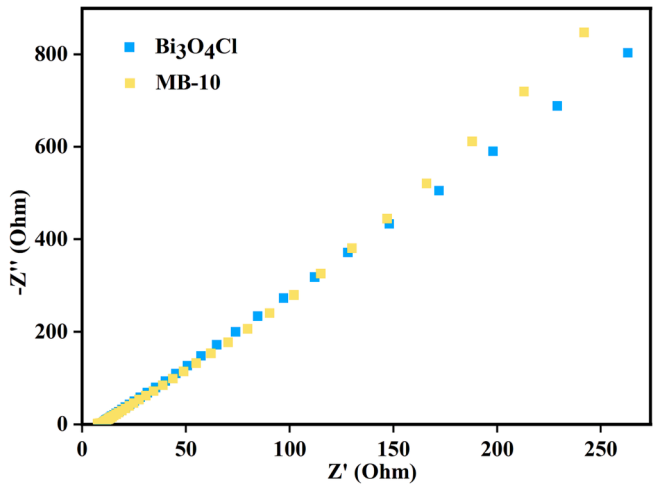

Fig. 9. EIS of Bi_3O_4Cl and MB-10.

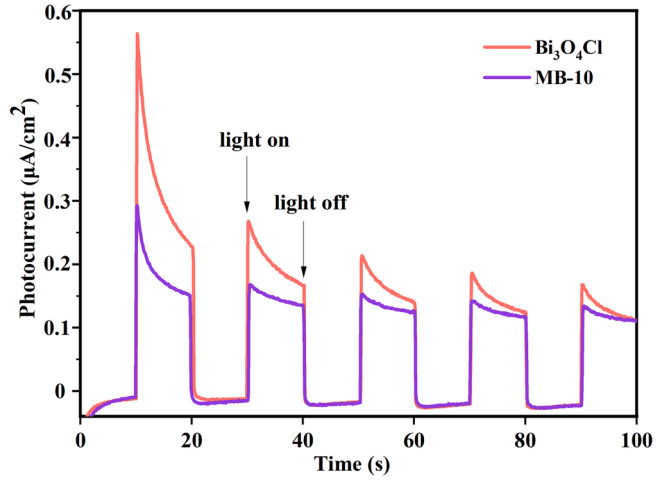

Fig. 10. Transient photocurrent response (I-t) of Bi_3O_4Cl and MB-10.

$Mn_xZn_{1-x}Fe_2O_4$.

3.4. Photoelectrochemical properties

Typically, the weaker the PL intensity is, the less the compound probability of photogenerated h^+ and e^- is, which results in the longer life period of photogenerated carriers. Steady-state photoluminescence (PL) is applied to explore the migration efficiency and segregation of photoinduced electron-hole pairs investigated in Fig. 8. Under photo-excitation, the $Bi_3O_4Cl/Mn_xZn_{1-x}Fe_2O_4$ composite photocatalyst showed a greater photocurrent response intensity than Bi_3O_4Cl, which indicates the higher photogenerated carrier recombination rate of the $Bi_3O_4Cl/Mn_xZn_{1-x}Fe_2O_4$ composite photocatalyst than Bi_3O_4Cl. Furthermore, the greater efficiency of electron-hole separation after coupling decreases the lifetime of light-generated holes and electrons, which confirmed the slightly weaker photocatalytic activity of the $Bi_3O_4Cl/Mn_xZn_{1-x}Fe_2O_4$ composite magnetic photocatalyst compared with pure Bi_3O_4Cl.

Fig. 9 shows the electrochemical impedance spectroscopy (EIS) analysis for Bi_3O_4Cl and the prepared $Bi_3O_4Cl/Mn_xZn_{1-x}Fe_2O_4$. Bi_3O_4Cl presents a smaller curvature radius than the $Bi_3O_4Cl/Mn_xZn_{1-x}Fe_2O_4$ composite photocatalyst, which demonstrates a better interfacial charge transfer and separation efficiency and exhibits a greater conductivity.

The TPR results of pristine Bi_3O_4Cl and $Bi_3O_4Cl/Mn_xZn_{1-x}Fe_2O_4$ are investigated in Fig. 10 by an electrochemical workstation. Irradiated by simulated sunlight and obtained energy, the electrons transformed, resulting to an instantaneous increase in the photocurrent density of the reaction system and reaching the peak. Notably, the lowest photocurrent density was observed in the absence of light. Furthermore, the transient photocurrent density of pristine Bi_3O_4Cl is 0.56 $\mu A \cdot cm^{-2}$, which was nearly 2 times that of $Bi_3O_4Cl/Mn_xZn_{1-x}Fe_2O_4$, proving the superior election mobility performance.

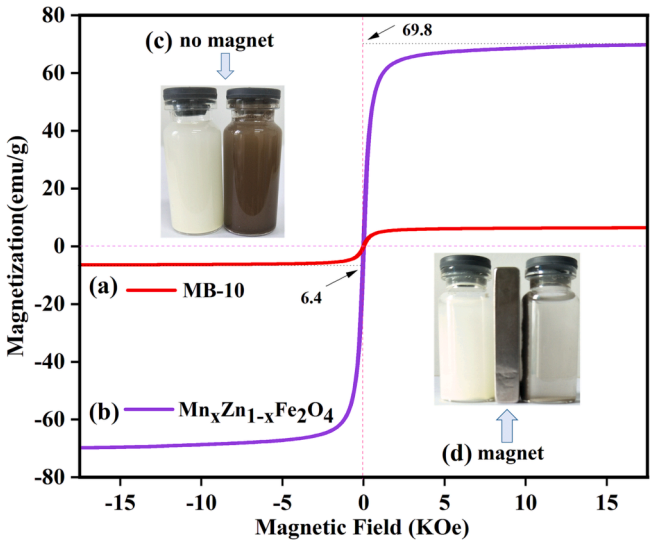

Fig. 11. **(a)-(b)** The magnetic hysteresis loops; **(c)** The suspension of Bi_3O_4Cl and MB-10; **(d)** The suspension of $Bi_3O_4Cl$and MB-10 under the magnetic field.

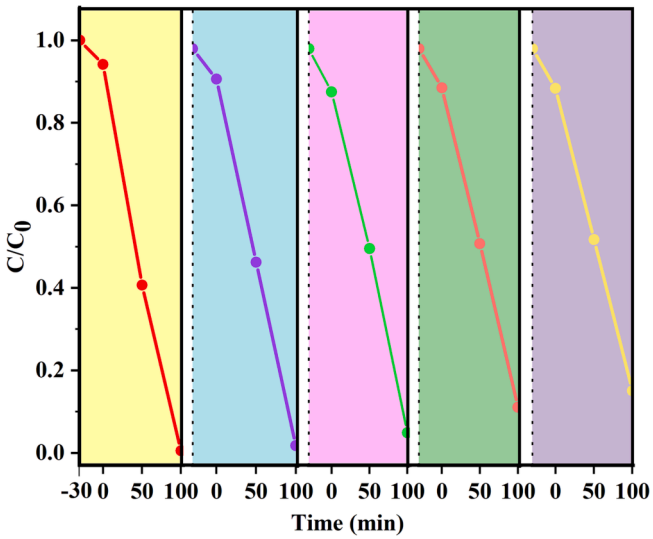

Fig. 12. Degradation rate of RhB on MB-10 after being recycled.

3.5. Magnetic properties

Fig. 11 illustrates the hysteresis loop diagrams of $Mn_xZn_{1-x}Fe_2O_4$ and $Bi_3O_4Cl/Mn_xZn_{1-x}Fe_2O_4$ composite photocatalysts. $Mn_xZn_{1-x}Fe_2O_4$ exhibited a greater hysteresis loop and coercivity, which can foster magnetic induction intensity and a lower hysteresis loss. Herein, the coercivity (Hc) of $Mn_xZn_{1-x}Fe_2O_4$ was 42 G, and the residual magnetization (Mr) was 6.8 emu/g. Compared with the saturation magnetization (Ms) of 70 emu/g owing to $Mn_xZn_{1-x}Fe_2O_4$, $Bi_3O_4Cl/Mn_xZn_{1-x}Fe_2O_4$ displayed a weaker Ms of 6.42 emu/g. The Mr of $Bi_3O_4Cl/Mn_xZn_{1-x}Fe_2O_4$ retained 0.52 emu/g, which indicates a lower $Mn_xZn_{1-x}Fe_2O_4$, and the calculation process was responsible for the weaker residual magnetization (Mr). Given an external magnetic field, Bi_3O_4Cl exhibited

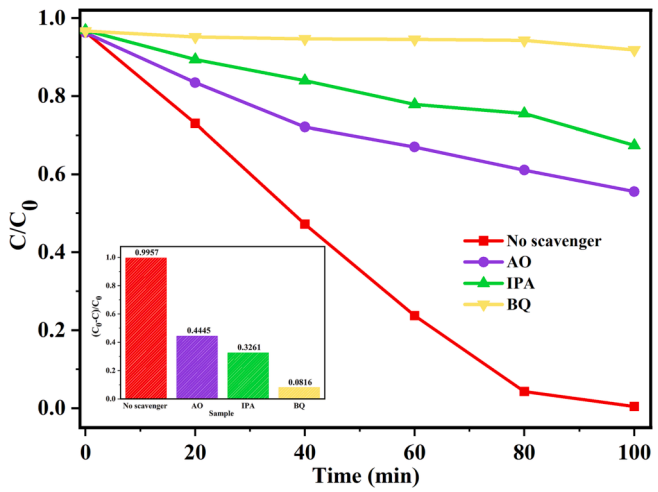

Fig. 13. Effect of radical scavengers on RhB photocatalytic degradation of MB-10.

no magnetism, while $Bi_3O_4Cl/Mn_xZn_{1-x}Fe_2O_4$ displayed an ideal magnetism sharply. Hence, $Bi_3O_4Cl/Mn_xZn_{1-x}Fe_2O_4$ could be regarded as a composite photocatalyst with excellent magnetic properties for recycling and magnetism.

3.6. Stability and recycling ability

The stability of the composite is proven by circular photodecomposition of RhB solution under the same conditions as presented in Fig. 12. Given an accurate weighing, the recovery of each catalyst was 91.3 %. After 5 cycles, no distinct deterioration could be observed in the degradation curves, and the recovery of the catalyst was 82.2 %, which verifies the excellent stability of the composites in RhB degradation.

3.7. Photocatalytic mechanism

Free radical capture experiments are prepared to reveal the main active substances by the samples investigated in Fig. 13. IPA (Isopropyl alcohol), BQ (benzoquinone) and AO (ammonium oxalate) were prepared in the experiment to detect hydroxyl radicals (·OH), photogenerated holes (h^+) and superoxide anion rabical ($\cdot O_2^-$), respectively. Confirming their effects on catalytic degradation in the reaction system. After adding AO, IPA and BQ, the degradation rate of RhB retained 44.5 %, 32.6 % and 8.2 %, respectively. This indicates the importance of h^+, ·OH and $^\bullet O_2^-$.

In addition, the band gap energies of the specimens could be initially evaluated under UV–vis DRS. The fitted E_g of Bi_3O_4Cl was estimated to be 3.05 eV. In addition, the E_{VB} values of Bi_3O_4Cl and $Mn_xZn_{1-x}Fe_2O_4$ were 3.43 eV and 1.17 eV, respectively. However, with E_{VB} higher than 2.3 eV, Bi_3O_4Cl fostered OH^- oxidation to ·OH(OH^-/·OH, 2.3 eV vs. NHE) by photogenerated holes (h^+) (Li et al., 2017). $Mn_xZn_{1-x}Fe_2O_4$ with weaker E_{VB} negatively contributed to the inability to oxidize OH^- to ·OH. Furthermore, compared with −0.33 eV, the lower E_{CB} of $Mn_xZn_{1-x}Fe_2O_4$ displayed perfect O_2 reduction to $^\bullet O_2^-$(O_2/ $^\bullet O_2^-$, −0.33 eV vs. NHE) (Fu et al., 2012), while Bi_3O_4Cl with a higher E_{CB} exhibited nothing on it. The Z-type heterojunction (Zhao et al., 2023; Zhao et al., 2023) $Bi_3O_4Cl/Mn_xZn_{1-x}Fe_2O_4$ is investigated in Fig. 14, which reveals the possible pathway to catalyse the mechanism. The intensive combination of e^- on Bi_3O_4Cl and h^+ on $Mn_xZn_{1-x}Fe_2O_4$ contributes to the Z-type heterojunction. The h^+ on Bi_3O_4Cl had two pathways, and some of them degraded RhB directly. Others effectively promoted OH^- oxidation to ·OH, which eliminated RhB later. Concurrently, the e^- on $Mn_xZn_{1-x}Fe_2O_4$ reduced O_2 to $^\bullet O_2^-$, confirming the duration of RhB under $^\bullet O_2^-$. The purpose and discussion of RhB degradation by the $Bi_3O_4Cl/Mn_xZn_{1-x}Fe_2O_4$ composite magnetic photocatalyst were exhibited under the reaction mechanism, which matches the results of free radical capture.

4. Conclusions

In summary, by the hydrothermal-roasting method, $Bi(NO_3)_3{\cdot}5H_2O$ and NaCl were used as raw materials, $Mn_xZn_{1-x}Fe_2O_4$ was used as the

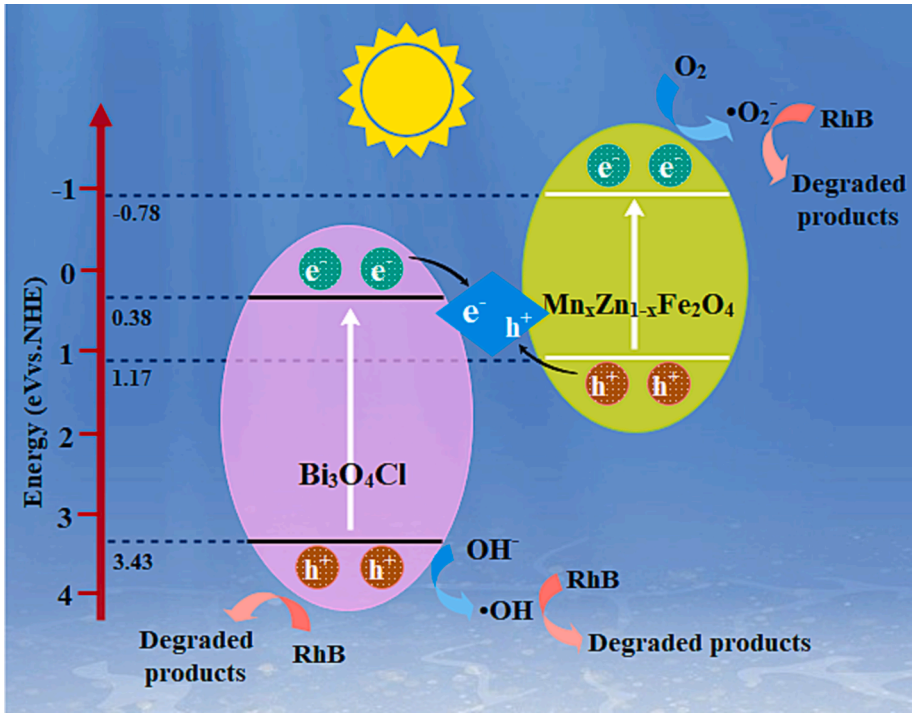

Fig. 14. Photocatalytic mechanism of RhB dye degradation over $Bi_3O_4Cl/Mn_xZn_{1-x}Fe_2O_4$.

magnetic substrate, and the $Bi_3O_4Cl/Mn_xZn_{1-x}Fe_2O_4$ composite magnetic photocatalyst was successfully fabricated. RhB was utilized as the target degradation to evaluate the performance of the photocatalysts, and the obtained $Bi_3O_4Cl/Mn_xZn_{1-x}Fe_2O_4$ photocatalyst exhibited an excellent photocatalytic behaviour, which could contribute to the doping of $Mn_xZn_{1-x}Fe_2O_4$ onto Bi_3O_4Cl. Since more active sites were provided, with a higher specific surface area, the $Bi_3O_4Cl/Mn_xZn_{1-x}Fe_2O_4$ photocatalyst was essential to the exhibition of higher adsorption of RhB. MB-10 exhibited fine magnetic recovery. In addition, an efficient preparation method is also proposed in this paper, which provides a simple and feasible approach for obtaining $Bi_3O_4Cl/Mn_xZn_{1-x}Fe_2O_4$ photocatalysts. Thus, an ideal potential application for the removal of environmental pollutants in the area of photocatalysis is available.

CRediT authorship contribution statement

Hailong Wang: Conceptualization, Resources, Writing – review & editing, Visualization, Supervision, Funding acquisition. **Dan Yang:** Writing – original draft, Visualization. **Longjun Xu:** Conceptualization, Resources, Writing – review & editing, Visualization, Supervision, Funding acquisition.

Declaration of competing interest

The authors declare that they have no known competing financial interests or personal relationships that could have appeared to influence the work reported in this paper.

Acknowledgements

This research was supported by the National Natural Science Foundation of China (NSFC, 51374259).

References

Acharya, S., Swain, G., Parida, K.M., 2020. MoS_2-mesoporous $LaFeO_3$ hybrid photocatalyst: Highly efficient visible-light driven photocatalyst. Int. J. Hydrogen. Energ. 45, 11502–11511. https://doi.org/10.1016/j.ijhydene.2020.01.158.

Akyüz, D., 2021. rGO-TiO_2-CdO-ZnO-Ag photocatalyst for enhancing photocatalytic degradation of methylene blue. Opt. Mater. 116, 111090 https://doi.org/10.1016/j.optmat.2021.111090.

Bao, E.P., Long, S., Zhang, S., et al., 2021. A ternary photocatalyst with double heterojunctionsfor efficient diesel oil degradation. ChemistrySelect 6, 3117–3125. https://doi.org/10.1002/slct.202004782.

Behnood, R., Sodeifian, G., 2021. Novel $ZnCo_2O_4$ embedded with S, N-CQDs as efficient visible-light photocatalyst. J. Photoch. Photobio. a 405, 112971. https://doi.org/10.1016/j.jphotochem.2020.112971.

Bhatt, P., Gangola, S., Bhandari, G., et al., 2021. New insights into the degradation of synthetic pollutants in contaminated environments. Chemosphere 268, 128827. https://doi.org/10.1016/j.chemosphere.2020.128827.

Cainglet, A., Tesfamariam, A., Heiderscheidt, E., 2020. Organic polyelectrolytes as the sole precipitation agent in municipal wastewater treatment. J. Environ. Manage. 271, 111002 https://doi.org/10.1016/j.jenvman.2020.111002.

Cheng, Y., Wu, T., Xu, L., et al., 2021. A novel visible-light-driven ternary magnetic photocatalyst $Mn_xZn_{1-x}Fe_2O_4$/C/CdS: fabrication, characterization and application. Mater. Chem. Phys. 262, 124308 https://doi.org/10.1016/j.matchemphys.2021.124308.

Cheng, Y., Wu, X., Xu, L., et al., 2021. Magnetically separable and recyclable ternary photocatalyst $Mn_xZn_{1-x}Fe_2O_4/BiVO_4/MnO_2$ with excellent photocatalytic activity. Vacuum 187, 110133. https://doi.org/10.1016/j.vacuum.2021.110133.

Cui, J., Zhang, Y., Zheng, Y., et al., 2021. Catalytic degradation of carbamazepine by a novel granular visible-light-driven photocatalyst activating the peroxydisulfate system. Chem. Eng. J. 421, 127867 https://doi.org/10.1016/j.cej.2020.127867.

Eddy, D.R., Ishmah, S.N., Permana, M.D., et al., 2021. Photocatalytic phenol degradation by silica-modified titanium dioxide. Appl.-Sci. 11, 9033. https://doi.org/10.3390/app11199033.

Frindy, S., Sillanpää, M., 2020. Synthesis and application of novel α-Fe_2O_3/graphene for visible-light enhanced photocatalytic degradation of RhB. Mater. Des. 188, 108461 https://doi.org/10.1016/j.matdes.2019.108461.

Fu, X., Tang, W., Ji, L., Chen, S., et al., 2012. V_2O_5 /Al_2O_3 composite photocatalyst: preparation, characterization, and the role of Al $_2O_3$. Chem. Eng. J. 180, 170–177. https://doi.org/10.1016/j.cej.2011.11.032.

Ghorai, K., Bhattacharjee, M., Mandal, D., et al., 2021. Facile synthesis of $CuCr_2O_4$/BiOBr nanocomposite and its photocatalytic activity towards RhB and tetracycline hydrochloride degradation under household visible LED light irradiation. J. Alloy. Compd. 867, 157947 https://doi.org/10.1016/j.jallcom.2020.157947.

Hu, X., Wang, G., Wang, J., et al., 2020. Step-scheme NiO/BiOI heterojunction photocatalyst for rhodamine photodegradation. Appl. Surf. Sci. 511, 145499 https://doi.org/10.1016/j.apsusc.2020.145499.

Jiang, Z., Hao, Y., Wu, T., et al., 2021. Carbon-coated $Mn_xZn_{1-x}Fe_2O_4$ as a magnetic substrate for $Zn_{0.8}Cd_{0.2}S$ applied in photocatalytic rhodamine B. Opt. Mater. 112, 110767 https://doi.org/10.1016/j.optmat.2020.110767.

Jing, H.-X., Li, L.-X., Huang, J., et al., 2020. Synthesis and characterization of ZnO-TiO_2/$CoFe_2O_4$ hollow photocatalyst: magnetic recovery and highly efficient photocatalytic performance. Funct. Mater. Lett. 13, 2051027. https://doi.org/10.1142/s1793604720510273.

Khalid, N.R., Mazia, U., Tahir, M.B., et al., 2020. Photocatalytic degradation of RhB from an aqueous solution using Ag_3PO_4/N-TiO_2 heterostructure. J. Mol. Liq. 313, 113522 https://doi.org/10.1016/j.molliq.2020.113522.

Li, Q., Chen, C., Li, C., et al., 2020. Ordered bicontinuous mesoporous polymeric semiconductor photocatalyst. ACS Nano 14, 13652–13662. https://doi.org/10.1021/acsnano.0c05797.

Li, X., Wan, T., Qiu, J., et al., 2017. In-situ photocalorimetry-fluorescence spectroscopy studies of RhB photocatalysis over Z-scheme g-C_3N_4@Ag@Ag_3PO_4 nanocomposites: a pseudo-zero-order rather than a first-order process. Appl. Catal. B-Environ. 217, 591–602. https://doi.org/10.1016/j.apcatb.2017.05.086.

Li, X., Ma, X., Lang, X., 2021. Blue light-powered hydroxynaphthoic acid-titanium dioxide photocatalysis for the selective aerobic oxidation of amines. J. Colloid Interface Sci. 602, 534–543. https://doi.org/10.1016/j.jcis.2021.06.008.

Li, J., Wu, X.Y., Pan, W.F., et al., 2018. Vacancy-rich monolayer BiO_{2-x} as a highly efficient UV, visible, and near-infrared responsive photocatalyst. Angew. Chem. Int. Ed. 57, 491–495. https://doi.org/10.1002/anie.201708709.

Li, J., Zang, H., Yao, S., et al., 2020. Photodegradation of benzothiazole ionic liquids catalyzed by titanium dioxide and silver-loaded titanium dioxide. Chinese J. Chem. Eng. 28, 1397–1404. https://doi.org/10.1016/j.cjche.2020.02.006.

Li, X., Zhang, J., Huo, Y., et al., 2021. Two-dimensional sulfur- and chlorine-codoped g-C_3N_4/CdSe-amine heterostructures nanocomposite with effective interfacial charge transfer and mechanism insight. Appl. Catal. B-Environ. 280, 119452 https://doi.org/10.1016/j.apcatb.2020.119452.

Lin, X., Huang, T., Huang, F., et al., 2006. Photocatalytic activity of a bi-based oxychloride Bi_3O_4Cl. J. Phys. Chem. B 110, 24629–24634. https://doi.org/10.1021/jp065373m.

Luo, H., Guo, J., Shen, T., et al., 2020. Study on the catalytic performance of $LaMnO_3$ for the RhB degradation. J. Taiwan. Inst. Chem. E. 109, 15–25. https://doi.org/10.1016/j.jtice.2020.01.011.

Ma, J., Shi, L., Hou, L., et al., 2020. Fabrication of graphene/$Bi_{12}O_{17}Cl_2$ as an effective visible-light photocatalyst. Mater. Rws. Bull. 122, 110690 https://doi.org/10.1016/j.materresbull.2019.110690.

Ma, J., Shi, L., Wang, Z., et al., 2020. 2D layered MoS_2 loaded on $Bi_{12}O_{17}Cl_2$ nanosheets: an effective visible-light photocatalyst. Ceram. Int. 46, 7438–7445. https://doi.org/10.1016/j.ceramint.2019.11.240.

Nabi, G., Majid, A., Riaz, A., et al., 2021. Green synthesis of spherical TiO_2 nanoparticles using Citrus Limetta extract: excellent photocatalytic water decontamination agent for RhB dye. Inorg. Chem. Commun. 129, 108618 https://doi.org/10.1016/j.inoche.2021.108618.

Niu, L., Hu, S., Ma, Y., et al., 2020. Fe-doped UiO-66 combined with $ZnIn_2S_4$ for adsorption and degradation of RhB under visible light. Nano 15, 1–11. https://doi.org/10.1142/s1793292020500897.

Pan, L., Ai, M., Huang, C., et al., 2020. Manipulating spin polarization of titanium dioxide for efficient photocatalysis. Nat. Commun. 11, 418. https://doi.org/10.1038/s41467-020-14333-w.

Pant, B., Prasad Ojha, G., Acharya, J., et al., 2021. Ag_3PO_4-TiO_2-Carbon nanofiber Composite: an efficient Visible-light photocatalyst obtained from eelectrospinning and hydrothermal methods. Sep. Purif. Technol. 276, 119400 https://doi.org/10.1016/j.seppur.2021.119400.

Senthil, R.A., Sun, M., Pan, J., et al., 2019. Facile fabrication of a new BiFeWO6/α-$AgVO_3$ composite with efficient visible-light photocatalytic activity for dye-degradation [J]. Opt. Mater. 92, 284–293. https://doi.org/10.1016/j.optmat.2019.04.046.

Sharma, E., Thakur, V., Sangar, S., et al., 2020. Recent progress on heterostructures of photocatalysts for environmental remediation. Mater. Today: Proc. 32, 584–593. https://doi.org/10.1016/j.matpr.2020.02.403.

Sohrabi, H., Ameri, E., 2015. Adsorption equilibrium, kinetics, and thermodynamics assessment of the removal of the reactive red 141 dye using sesame waste [J]. Desalin. Water Treat. 57 (38), 18087–18098. https://doi.org/10.1080/19443994.2015.1087345.

Sun, M., Senthil, R., Pan, J., et al., 2018. A facile synthesis of visible-light driven rod-on-rod like α-FeOOH/α-$AgVO_3$ nanocomposite as greatly enhanced photocatalyst for degradation of rhodamine B [J]. Catalysts 8 (9). https://doi.org/10.3390/catal8090392.

Talreja, N., Afreen, S., Ashfaq, M., et al., 2021. Bimetal (Fe/Zn) doped BiOI photocatalyst: an effective photodegradation of tetracycline and bacteria. Chemosphere 280, 130803. https://doi.org/10.1016/j.chemosphere.2021.130803.

Wang, Y., Kang, C., Li, X., et al., 2021. Ag NPs decorated C-TiO2/Cd0.5Zn0.5S Z-scheme heterojunction for simultaneous RhB degradation and Cr(VI) reduction. Environ. Pollut. 286, 117305 https://doi.org/10.1016/j.envpol.2021.117305.

Wang, R., Xu, M., Xie, J., et al., 2020. A spherical TiO_2-Bi_2WO_6 composite photocatalyst for visible-light photocatalytic degradation of ethylene. Colloid Surf. a 602, 125048. https://doi.org/10.1016/j.colsurfa.2020.125048.

Xu, B., Gao, Y., Li, Y., et al., 2020. Synthesis of Bi_3O_4Cl nanosheets with oxygen vacancies: the effect of defect states on photocatalytic performance. Appl. Surf. Sci. 507, 144806 https://doi.org/10.1016/j.apsusc.2019.144806.

Ye, S., Chen, Y., Yao, X., et al., 2021. Simultaneous removal of organic pollutants and heavy metals in wastewater by photoelectrocatalysis: a review. Chemosphere 273, 128503. https://doi.org/10.1016/j.chemosphere.2020.128503.

Yuan, Y., Guo, R.T., Hong, L.F., et al., 2022. Fabrication of a dual S-scheme $Bi_7O_9I_3$/g-C_3N_4/Bi_3O_4Cl heterojunction with enhanced visible-light-driven performance for phenol degradation. Chemosphere 287, 132241. https://doi.org/10.1016/j.chemosphere.2021.132241.

Zhang, J., Yang, Z., Wang, L., et al., 2020. Carbon covered Ag and Bi nanoparticles uniformly dispersed in porous carbon matrix: synergistic effect for removal of RhB. Mater. Lett. 275, 128099 https://doi.org/10.1016/j.matlet.2020.128099.

Zhao, C., Li, X., Yue, L., et al., 2023. $Bi_4O_5Br_2$ nanoflower and $CdWO_4$ nanorod heterojunctions for photocatalytic synthesis of ammonia [J]. ACS Appl. Nano Mater. 6 (17), 15709–15720. https://doi.org/10.1021/acsanm.3c02504.

Zhao, C., Li, X., Yue, L., et al., 2023. Fabrication of novel BiPO4/Bi4O5Br 2 heterojunctions for improving photoactivity in N2 fixation and dye degradation [J]. Mater. Res. Bull. 2023 (167), 112377 https://doi.org/10.1016/j.materresbull.2023.112377.

Zhao, C., Li, X., Yue, L., et al., 2023. One-step preparation of novel Bi-Bi2O3/CdWO4 Z-scheme heterojunctions with enhanced performance in photocatalytic NH3 synthesis [J]. J. Alloy. Compd. 2023 (968), 171956 https://doi.org/10.1016/j.jallcom.2023.171956.

Zhao, T., Qian, R., Zhou, G., et al., 2021. Mesoporous WO_3/TiO_2 spheres with tailored surface properties for concurrent solar photocatalysis and membrane filtration. Chemosphere 263, 128344. https://doi.org/10.1016/j.chemosphere.2020.128344.

Zhou, C.Y., Lai, C., Xu, P., et al., 2018. In Situ grown AgI/$Bi_{12}O_{17}Cl_2$ heterojunction photocatalysts for visible light degradation of sulfamethazine: efficiency, pathway, and mechanism. ACS Sustain. Chem. Eng. 6, 4174–4184. https://doi.org/10.1021/acssuschemeng.7b04584.

Ziental, D., Czarczynska-Goslinska, B., Mlynarczyk, D.T., et al., 2020. Titanium dioxide nanoparticles: prospects and applications in medicine. Nanomaterials-Basel 10, 387. https://doi.org/10.3390/nano10020387.